



**HAL**  
open science

**Perovskite nanostructures assembled in molten salt  
based on halogen anions KX (X = F, Cl and Br):  
Regulated morphology and defect-mediated  
photocatalytic activity**

Reshalaiti Hailili, Chuanyi Wang, Eric Lichtfouse

► **To cite this version:**

Reshalaiti Hailili, Chuanyi Wang, Eric Lichtfouse. Perovskite nanostructures assembled in molten salt based on halogen anions KX (X=F, Cl and Br): Regulated morphology and defect-mediated photocatalytic activity. *Applied Catalysis B: Environmental*, 2018, 232, pp.531-543. 10.1016/j.apcatb.2018.03.075 . hal-02064809

**HAL Id: hal-02064809**

**<https://hal.science/hal-02064809>**

Submitted on 12 Mar 2019

**HAL** is a multi-disciplinary open access archive for the deposit and dissemination of scientific research documents, whether they are published or not. The documents may come from teaching and research institutions in France or abroad, or from public or private research centers.

L'archive ouverte pluridisciplinaire **HAL**, est destinée au dépôt et à la diffusion de documents scientifiques de niveau recherche, publiés ou non, émanant des établissements d'enseignement et de recherche français ou étrangers, des laboratoires publics ou privés.

# Perovskite nanostructures assembled in molten salt based on halogen anions KX (X = F, Cl and Br): Regulated morphology and defect-mediated photocatalytic activity



Reshalaiti Hailili<sup>a,b,1</sup>, Chuanyi Wang<sup>a,c,\*</sup>, Eric Lichtfouse<sup>d</sup>

<sup>a</sup>Laboratory of Environmental Sciences and Technology, Xinjiang Technical Institute of Physics & Chemistry, Key Laboratory of Functional Materials and Devices for Special Environments, Chinese Academy of Sciences, Urumqi 830011, China

<sup>b</sup>The Graduate School of Chinese Academy of Science, Beijing 100049, China

<sup>c</sup>School of Environmental Science and Engineering, Shaanxi University of Science and Technology, Xi'an, Shaanxi 710021, China

<sup>d</sup>CEREGE, University of Aix-Marseille, Aix en Provence, 13100, France

## ABSTRACT

### Keywords:

Visible light active perovskite  
Oxygen vacancy  
Molten salt synthesis  
Halogen anions  
Tetracycline degradation

Defect engineering of semiconductors provides an effective strategy for improving photocatalytic performance without doping alien elements. Understanding the defect and defect-related photocatalytic activity of semiconductors could lead to new horizon in the rational design of photocatalysts for practical applications. Herein, novel oxygen-deficiency contained perovskite  $\text{CaCu}_3\text{Ti}_4\text{O}_{12}$  with tunable structures of cube, nanoparticle and octahedron were for the first time synthesized via a feasible molten salt reaction approach depending on halogen anions of employed salts KX (X = F, Cl and Br). Formation mechanisms of the different structures were revealed on the basis of innate characters of the selected halide anions. Assorted shapes display strong visible light absorption, which is interconnected with Ti displacement and oxygen deficiency. The photocatalytic performances of those three homologues were evaluated by an antibiotic degradation under visible light illumination. A superior photoefficiency is achieved for octahedron shaped crystal, which reduces 95.86% total organic carbon within 60 min and exhibits the reaction rate normalized to surface area of  $1.261 \times 10^{-2} \text{ g min}^{-1} \text{ m}^{-2}$ , approximately 3.687 and 3.474 times larger than its counterparts. The outstanding degradation efficiency is ascribed to the synergetic roles of effective charge transfer, oxygen deficiencies and critical roles of active radicals resulting in carrier separation and efficiency enhancement. This work provides fundamental understanding of the morphology tailoring and defect controlling towards exploring new generation of visible light photocatalysts for environment and energy applications.

## 1. Introduction

Semiconductor based photocatalysis is a promising method to address two of the largest current crises: energy shortage and environment pollution [1,2]. Of the particular interest is to alleviate organic contaminants from water and atmosphere, where pollutants have high toxicity at very low concentration (ppm) [2]. To improve light harvesting efficiency of photocatalysts, the actual challenges are better sunlight utilizations and understanding the reaction mechanisms. Many successful state-of-the-art catalysts have been developed for photocatalysis, e.g.,  $\text{TiO}_2$ , due to their outstanding stability, low-cost, excellent photocatalytic activity and environment-benign property [1–5]. Unfortunately, the dissatisfactory reaction yields and finite light

absorption hinder their practical applications because of the rapid carrier recombination and inappropriate electronic band gap. Thus, sufficient visible light absorption and effective charge carrier separation are essential that play important roles in wide range of photolysis such as efficiently harvesting solar light into energy, while crystal structures and surface characters of semiconductors are critical for photocatalytic reaction.

Defects in the photocatalysts would affect solar conversion efficiencies by influencing light absorption, rapid depletion of photo-induced carriers and various surface metrics [6–8]. Stimulated by defect mediating and morphology tailoring of crystal characteristics (atomic arrangements, band configurations and alignments), the regulating crystal structures to improve photoactivity of semiconductors is

\* Corresponding author at: Laboratory of Environmental Sciences and Technology, Xinjiang Technical Institute of Physics & Chemistry, Key Laboratory of Functional Materials and Devices for Special Environments, Chinese Academy of Sciences, Urumqi 830011, China.

E-mail addresses: [cywang@ms.xjb.ac.cn](mailto:cywang@ms.xjb.ac.cn), [wangchuanyi@sust.edu.cn](mailto:wangchuanyi@sust.edu.cn) (C. Wang).

<sup>1</sup> These authors contributed equally to this work.

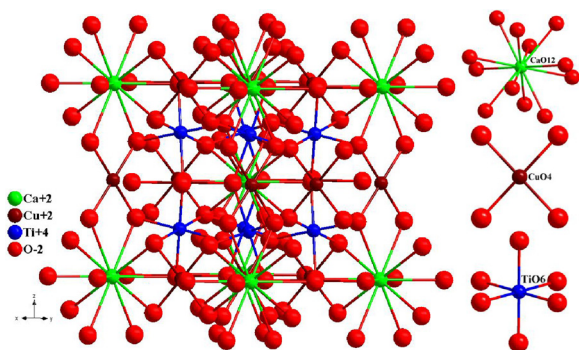


Fig. 1. Crystal structure of cubic perovskite  $\text{CaCu}_3\text{Ti}_4\text{O}_{12}$  in the unit cell (ICSD No. 95714) shows  $\text{CaO}_{12}$ , planar  $\text{CuO}_4$  clusters and  $\text{TiO}_6$  units.

a current topic of great interest [9]. Actually, defects in the crystal lattice, even if in infinitesimal amounts, result in newly formed disordered structure at specific preparation conditions and influence reaction pathways [8]. Importantly, defects such as oxygen deficiencies act as active reaction sites by reacting with surface adsorbed oxygen molecules leading to formation of doubly ionized ( $\text{O}_2^{2-}$ ) or singly ionized ( $\text{O}_2^-$ ) species on the surface of catalyst, thus promote carrier migration or directly involve the photocatalytic reactions [9]. Therefore, carefully designing photocatalysts with defects would cause drastic changes in photocatalytic activity due to improved light absorption, good conductivity and reduced charge carrier recombination.

Emerging as a newly explored visible light catalyst, the double perovskite  $\text{CaCu}_3\text{Ti}_4\text{O}_{12}$  is one of the fundamentally important materials that has drawn much attention recently [10–14]. The  $\text{CaCu}_3\text{Ti}_4\text{O}_{12}$  is mostly studied for dielectric property, which is arisen from its well conductivity and instinct defect in the local structure. The perfect crystal of  $\text{CaCu}_3\text{Ti}_4\text{O}_{12}$  consists of  $\text{CaO}_{12}$ , square planar  $\text{CuO}_4$  ( $\text{Cu}^{2+}$ ) units and octahedron  $\text{TiO}_6$  ( $\text{Ti}^{4+}$ ) clusters in the unit cell, in which both Ca and Cu are superimposed on the same crystallography positions (Fig. 1). Herein, we choose  $\text{CaCu}_3\text{Ti}_4\text{O}_{12}$  as a potential environmental photocatalyst based on the following justifications: (i) Incorporation of earth abundant, open-shell cations ( $\text{Cu}^{2+}$ ) in the instinct structure could enlarge light absorption range and exhibit much superior visible light activity than that of well-known photocatalysts consist of cation contained closed-shell structure [15,16]; (ii) The valence band level of  $\text{TiO}_2$  is composed of O 2p occupied orbitals, while its conduction band is comprised of Ti 3d states, which give rise to greatly decreased photocatalytic reaction. Compared with widely studied metal oxides e.g.,  $\text{TiO}_2$ , the presence of narrow band gap (Cu 3d + O 2p) of planar tetra-coordinated oxygen containing  $\text{CuO}_4$  in  $\text{CaCu}_3\text{Ti}_4\text{O}_{12}$  extends the light absorption and is favourable for redox reactions; (iii) Taking advantages of stepwise ionization of flux agents during molten salt synthesis, the planar defects from  $\text{CuO}_4$  units can be controlled and distortion of the  $\text{TiO}_6$  clusters cause a displacement in Ti–O–Ti bonds leading to disorder structures, as a result, various deficiencies (oxygen vacancy and metal defects of  $\text{Cu}^+$  and  $\text{Ti}^{3+}$ ) ubiquitous in  $\text{CaCu}_3\text{Ti}_4\text{O}_{12}$ , meanwhile its morphology can be effectively regulated [12]. However, both understanding of morphology controlled synthesis and defect induced visible light driven photocatalytic performances of  $\text{CaCu}_3\text{Ti}_4\text{O}_{12}$  are still in its infancy and corresponding reaction mechanisms are remain elusive. All aforementioned features inspire us to explore structure-performance correlations of this material on photocatalytic reaction.

Herein, we present shaped-controlled perovskite catalyst  $\text{CaCu}_3\text{Ti}_4\text{O}_{12}$  prepared in molten salts based on the halogen anions of the selected flux agents KX (X = F, Cl and Br). It is found that variations of utilized salt compositions play significant roles in the evolution of assorted morphologies and various crystal defects, especially the anions of salts are the crucial factor for the nanocrystals directional growing.

As-obtained  $\text{CaCu}_3\text{Ti}_4\text{O}_{12}$  samples exhibit defect associated photocatalytic performances for pollutant degradation. The decomposition mechanisms are proposed on the basis of unique crystal structures and defects. As we know, this is the first investigation of halogen anion effects of employed salts on morphology/defect regulations of double structured perovskite  $\text{CaCu}_3\text{Ti}_4\text{O}_{12}$  and its defect induced photocatalytic activity.

## 2. Experimental

### 2.1. Preparation method

In general, perovskite compounds are composed of two or more simple oxides with high melting points. Therefore, very high temperature and long calcination time is required to achieve successful diffusion of atoms and preparing pure phases, especially for metal oxides, whose photocatalytic properties are strongly influenced by many factors such as surface area, crystallite size, exposed crystal facet, morphology and defect concentration [17,18]. All these characters are directly associated with syntheses and processing routes. Therefore, exploring the aspects which manipulate properties of nanostructures is crucial and significant in many ways in the investigation of nanomaterials. Various synthetic methods have been proposed for synthesis and morphology evolution of  $\text{CaCu}_3\text{Ti}_4\text{O}_{12}$  such as solid-state reaction, sol-gel synthesis and co-precipitation etc., though proved to be undesirable since as-obtained sample suffers from phase impurity and low surface area [19–21]. In contrast to these techniques, molten salt synthesis is known as a booming, cost-effective and feasible approach aiming at surface modification and morphology controlled synthesis [12,22–24]. This environmentally friendly synthetic method had been applied to the fabrication of wide range of perovskites, i.,  $\text{K}_{1.9}\text{Na}_{0.1}\text{Ta}_2\text{O}_6$ ,  $\text{Bi}_4\text{Ti}_3\text{O}_{12}$ ,  $\text{SrBi}_2\text{Ta}_2\text{O}_9$  and  $\text{Pb}_2\text{Bi}_4\text{Ti}_5\text{O}_{18}$ , etc., for their diverse applications [22–25]. Very recently, taking advantages of the process by stepwise ionization of molten salts, a comprehensive study on morphology tailoring and visible light photocatalytic activity of  $\text{CaCu}_3\text{Ti}_4\text{O}_{12}$  was investigated [12]. Further study revealed that a systematic investigation on synthetic conditions (calcination time and temperature) during the molten salt synthesis were critical for morphology tailoring and defect tuning [26]. Additionally, Cl ions from salt KCl gave rise to unique octahedron shapes, dual defects and coexposed ( $\{001\}$ ,  $\{111\}$ ) facets of  $\text{CaCu}_3\text{Ti}_4\text{O}_{12}$  during the molten salt reaction [27]. Therefore, it can be assumed that well-controlled reaction conditions during the molten salt synthesis are beneficial for morphology and defect tuning in  $\text{CaCu}_3\text{Ti}_4\text{O}_{12}$  as well as surface characters of desired catalysts. However, essentially no studies report the salt dependent morphology evolution by altering halogen anions of employed salt and microstructure-defect-performance correlations of  $\text{CaCu}_3\text{Ti}_4\text{O}_{12}$ . As such, one-step, effective molten salt synthesis was selected to examine influence of halogen anions of molten salt KX (X = F, Cl and Br) on the crystal structure and corresponding photocatalytic performance of  $\text{CaCu}_3\text{Ti}_4\text{O}_{12}$ .

### 2.2. Catalyst preparation

All the reagents were of analytical grade purity and applied as received without further purification. Calcium copper titanate catalysts were synthesized via molten salt approach using metal oxides and salt agents of KX (X = F, Cl and Br) as starting raw materials. In a typical procedure, the stoichiometrical amounts of the metal oxides e.g., calcium oxide (0.0049 mol, 99.8%), copper (II) oxide (0.0146 mol, 99.8%) and titanium dioxide (0.019 mol, 99.9%, from Sigma-Aldrich) were placed into an agate mortar and grinded for about 60 min to obtained well-grinded mixture, followed by the addition of selected salts of KX (X = F, Cl and Br, purchased from Tianjin Bodi Chemical Industry Co., Ltd.). The mixture of metal precursors and inorganic salts was placed into the ball mill, then, continuously grinded for about 240 min.

Following by this procedure, the obtained mixture was dried in the heating oven for 10 min to remove alcohol, calcinated in the corundum crucible for 300 min at 800 °C and cooled to indoor temperature with a rate of 1 °C min<sup>-1</sup>. The gained substances were washed in mixture of absolute ethanol and deionized water (18 MΩ cm<sup>-1</sup>, resistivity). At the final step, desired samples were dried at 80 °C for 300 min, grinded and collected for further characterizations and activity evaluations.

### 2.3. General remarks

The crystal morphologies of the catalysts were investigated by Scanning Electron Microscope (SEM) on a Hitachi S-3500N. The X-ray Power Diffraction (XRD) measurement was carried out on a Bruker D8 ADVANCE X-ray diffractometer in the angular range of  $2\theta = 5^\circ\text{--}80^\circ$  with a scan step width of 0.02° and a fixed counting time of 1 s/step using CuK $\alpha$  radiation ( $\lambda = 1.5418 \text{ \AA}$ ). XRD pattern simulation was also generated using Mercury 3.0.17 software for structure comparison. For further phase determination, the element composition was examined with an Energy-Disperse X-ray instrument EDX G2T20136–5. The light absorption properties of per 40.0 mg samples were measured on an UV–vis spectrophotometer (Shimadzu Solidspec–3700 DUUV) at room temperature over the wavelength range of 200 nm–800 nm. The BaSO<sub>4</sub> was applied as a reference material for base line correction. The Fourier Transform Infrared (FTIR) Spectra were recorded from KBr pellets containing ca. 1.0 mg of the catalyst in the range from 4000 cm<sup>-1</sup> to 400 cm<sup>-1</sup> with resolution of 2 cm<sup>-1</sup> on Bruker Optics TENSOR 27 Fourier Transform Infrared Spectrometer. The electron paramagnetic resonance (EPR) spectra were collected at 4–298 K with a Bruker E500 instrument working under the X-band and equipped with an Oxford cryostat. In a typical procedure, per 20.0 mg of samples were placed inside a spectroscopically pure quartz cell with greaseless stopcock and sent into the EPR cavity with fixed depth. All the spectra were recorded at 100 K and the *g* values were determined by calibration with DPPH (Bruker spectrometer) standard. The surface areas of 30.0 mg samples were determined from the Brunauer–Emmett–Teller (BET) method after outgassed at 180 °C for 3 h. The N<sub>2</sub> adsorption–desorption isotherms were recorded with a QUADRASORB IQ, Quantachrome Instrument Corp, and the sample's corresponding surface areas were calculated from the linear part of the multi-point BET plot.

### 2.4. Photocatalytic activity evaluations

The photocatalytic decomposition activity of as-obtained samples were tested by choosing tetracycline as a probe molecule. The obtained products of 40.0 mg were placed into a tubular quartz reactor of tetracycline aqueous solution (100 mL,  $1.0 \times 10^{-5} \text{ mol L}^{-1}$ ). The mixture was placed in a beaker, stirred and then positioned in dark to establish adsorption equilibrium on the catalyst surface. For light source, the 300 W Xe lamp (PLS-SXE300, Perfect Light Company, Beijing, China) was used. The power intensity was measured to be 400 mW cm<sup>-2</sup>. In the degradation reaction, the reactor was surrounded with light and irradiated the sample-tetracycline aqueous solution at room-temperature. After the reaction, the sample was withdrawn at given duration and centrifuged at 9000 r m<sup>-1</sup> for 15 min to discard any sediment. The tetracycline concentration was monitored and determined through a wavelength scan on an UV–vis spectrophotometer (UV–1800, Shimadzu, Japan) at the maximum absorption of 355.0 nm, then, absorption spectra and the tetracycline degradation ratio were obtained.

### 2.5. Catalyst stability test

The catalyst's long-term efficiency and structure stability during the photocatalytic degradation was tested by running six cycle tetracycline decompositions. In a detail procedure, a fixed quantity of desired catalyst (40.0 mg) was placed in 100 mL of  $1.0 \times 10^{-5} \text{ mol L}^{-1}$  tetracycline aqueous solution and degradation experiment was performed

with the same procedure as mentioned in the activity test. For six cycle successive decompositions, the catalyst was separated by centrifuging it after the prior cycle and recovered from the centrifuge tube into a beaker with a fresh tetracycline solution ( $1.0 \times 10^{-5} \text{ mol L}^{-1}$ ). Then, the tetracycline-catalyst contained suspension was subjected to magnetic stirring in the dark and exposed to visible light irradiation for the next cyclic test. The tetracycline concentration was obtained from UV–vis absorption analysis with the same measurement method as applied in the activity evaluation experiment. After six run successive tests, the samples were gathered for XRD and FTIR measurements to confirm structure stability.

### 2.6. Mineralization degree assessment

The centrifuged samples were further analyzed by total organic carbon (TOC) measurement on a vario TOC (Elementar, Germany) analyzer. The standard potassium hydrogen phthalate solution was used to calibrate the standard curve, and the calculated *R* value is about 0.9995.

### 2.7. Photoelectrochemical measurement

Photocurrent measurements were carried out using an electrochemical analyzer (Chenhua Instruments Co., Shanghai) with conventional three-electrodes: the ITO/photocatalysts (with an area of 1.0 cm × 1.0 cm as a photoanode) electrodes as the working electrode, a Pt wire as the counter electrode and saturated calomel electrode Ag/AgCl (saturated KCl) as a reference electrode and visible light from 300 W Xe lamp used as light source. The 0.1 mol L<sup>-1</sup> Na<sub>2</sub>SO<sub>4</sub> was used as electrolyte which was filled in a single-compartment quart cell.

### 2.8. Quantitative experimentsof active species determination

The quantitative radical trapping tests were conducted to confirm main contributions of active species. A selected trapping agents were introduced into the suspension and stirred before the degradation experiments, which were carried out at the identical reaction conditions with photocatalytic tests. In this study, series of trapping agents were used, for instance, isopropyl alcohol (IPA) to detect hydroxide ( $\cdot\text{OH}$ ), silver nitrate (AgNO<sub>3</sub>) as an electron ( $e^-$ ), *P*-benzoquinone (PBQ) to capture superoxide ( $\cdot\text{O}_2^-$ ), and ammonium oxalate (AO) as a hole ( $h^+$ ) scavenger, respectively.

### 2.9. Detection of active radicals by electron spin resonance (ESR) measurements [28]

The active radicals involved photocatalytic reaction were examined by ESR measurements, in which the spin lables of 5,5–dimethyl-1-pyrroline *N*-oxide (DMPO), 2, 2, 6, 6–tetramethylpiperidine-1-oxyl (TEMPO) and 1–hydroxy-3-carboxy-2, 2, 5, 5-tetramethylpyrrolidine (CPH) were applied to confirm effective formation of active radicals such as  $\cdot\text{O}_2^-$ ,  $\cdot\text{OH}$ ,  $e^-$  and  $h^+$ , respectively. In detail, per 10.0 mg catalyst was dispersed in 1.5 mL of water or methanol (HPLC grade) and then was vigorously stirred for 30 s followed by the addition of 25.0 μL DMPO/TEMPO, 15.0 μL DMPO (for detection  $\cdot\text{OH}$ ) and 10.0 μL CPH solution. The obtained mixture was analyzed by electron paramagnetic resonance (EPR) after irradiated with a 300 W Xe lamp.

## 3. Results and discussion

### 3.1. Synthesis and characterization of photocatalysts

#### 3.1.1. Morphology and formation mechanism of photocatalyst

The morphological features of as-obtained samples are observed by SEM as shown in Fig. 2, in which ascertained microstructures are rather different based on the compositions of employed salts KX (X = F, Cl and Br). When

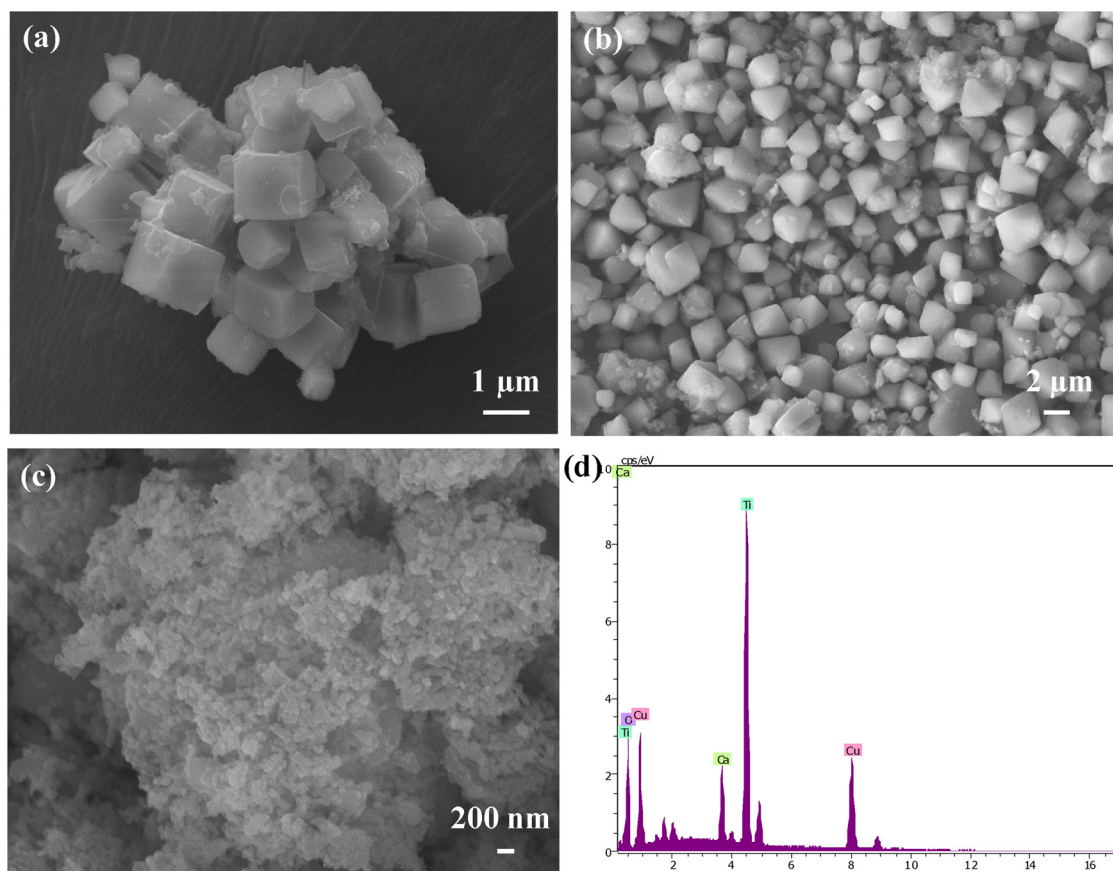


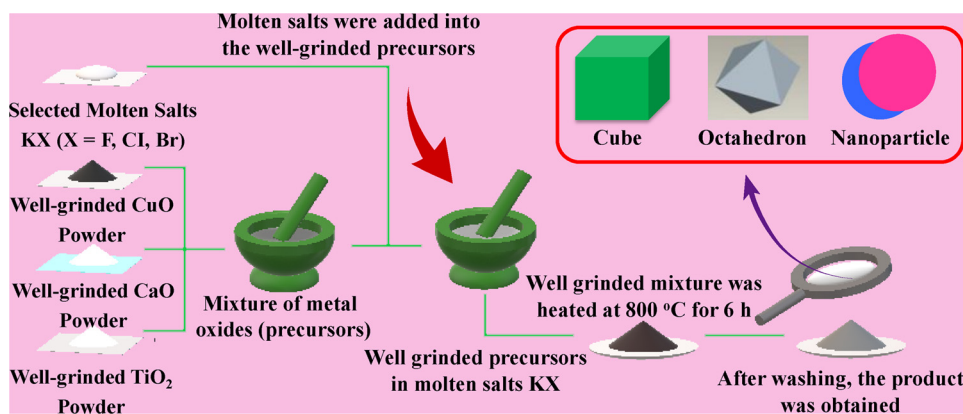
**Fig. 2.** (a) Cube shaped  $\text{CaCu}_3\text{Ti}_4\text{O}_{12}$  obtained with the assistance of the molten salt KF; (b) Uniformly dispersed  $\text{CaCu}_3\text{Ti}_4\text{O}_{12}$  octahedrons prepared in the molten salt KCl; (c) High yield and uniform  $\text{CaCu}_3\text{Ti}_4\text{O}_{12}$  nanoparticles fabricated in the molten salt KBr; (d) EDS spectrum shows merely Ca, Cu, Ti and O compositions of nanoparticles, evidences the sample is  $\text{CaCu}_3\text{Ti}_4\text{O}_{12}$ .

the molten salt KF was applied into synthesis, very uniform cube shaped  $\text{CaCu}_3\text{Ti}_4\text{O}_{12}$  crystals (side length  $\times$  width  $\times$  height  $\approx 1 \times 1 \times 1 \mu\text{m}$ ) with the product yields of 97% were observed (Fig. 2a). As the increasing of reaction temperature to the melting point of salt agent during the reaction, the utilized KF salt ionized to  $\text{K}^+$  and  $\text{F}^-$ , which could be adsorbed on the surface or different sites of  $\text{CaCu}_3\text{Ti}_4\text{O}_{12}$  to form cube shaped crystal with specific exposed facets, e.g., (001) facet without using any templates. Same results are obtained in (001) facet inorganic materials though with structure directing agents, for instance HF [29–31]. It is worth to pointed out that a morphology controlled synthesis of photocatalytic materials should not be constrained merely on the surfactant or shaped controlled agent such as HF.

In fact, the varied salt compositions may hinder or even reverse the expected morphology tailoring in the studied  $\text{CaCu}_3\text{Ti}_4\text{O}_{12}$  samples, which was further testified by altering the salt system into KCl. Evidently, when the anions of KX changed to  $\text{Cl}^-$  (KCl), the obtained product was comprised of highly uniformed octahedrons with clean crystal surface and high yield of products ( $\sim 95\%$ , yields) as exhibited in Fig. 2b. Nanostructured photocatalysts with clean surface like as-obtained octahedrons are highly desired for further investigation on their photoactivity as well as other property at the nanoscience as building functional components. Fig. 2c exhibits the microstructures of sample obtained with the assistance of molten salt KBr. The uniformed nanoparticles (10 nm–20 nm) with high yield of products ( $\sim 90\%$ ) are observed. Reducing particle size of a photocatalysts shortens the transferring charge carrier pathway, thus leading to effective carrier separation and consequently the enhanced photocatalytic effectiveness. Notably, photocatalysts synthesized by molten salt method give high yields of product and relatively pure phase merely depend on introducing trace amounts of inorganic salts as revealed by energy

dispersive spectroscopy (EDS) analysis, demonstrating phase purity of the prepared sample as it comprised only Ca, Cu, Ti and O elements (Fig. 2d).

Generally, there are varieties of synthetic parameters that have strong impact on growth behaviour of nanomaterials during the molten salt synthesis. Crucial factors, such as salt amounts, calcination temperature and time, mole ratio of salts as well as the crystal structures and ions of introduced salts should be considered to investigate the nucleation and salt dependent growth mechanism of  $\text{CaCu}_3\text{Ti}_4\text{O}_{12}$ . Importantly, the main factor is the choice of salt compositions. Herein, the common used salts KX ( $X = \text{F}, \text{Cl}$  and  $\text{Br}$ ) were selected as salt agents and other reaction conditions (reaction time, temperature and molar ratio) were kept the same. The sole significant difference in preparation condition was the halogen anions (F, Cl and Br). Therefore, variations in the morphologies of  $\text{CaCu}_3\text{Ti}_4\text{O}_{12}$  can only be ascribed to the shifting salt compositions, e.g., effects of halogen anions of KX ( $X = \text{F}^-, \text{Cl}^-$  and  $\text{Br}^-$ ), which contribute to high yields and uniformly dispersed diverse morphologies during the synthesis. Besides, formation of these morphologies can be explained in terms of different viscosity, polarity, vapor pressure, mobility or crystal structures of the utilized molten salts. For instance, the employed molten salts KX are gradually ionized as the reaction temperature is increased to their melting points and released cations ( $\text{K}^+$ ) and various anions ( $\text{F}^-, \text{Cl}^-$  and  $\text{Br}^-$ ), which could adsorb and interact with catalyst's surface. It should be pointed out that the studied photocatalyst  $\text{CaCu}_3\text{Ti}_4\text{O}_{12}$  is an  $n$  type of semiconductor with negative charges, and selected salt anions ( $\text{F}^-, \text{Cl}^-$  and  $\text{Br}^-$ ) exhibit assorted electronegativities:  $\chi_{\text{F}} (10.4) > \chi_{\text{Cl}} (8.30) > \chi_{\text{Br}} (7.59)$  and ionic radii:  $R_{\text{Br}} (196 \text{ pm}) > R_{\text{Cl}} (181 \text{ pm}) > R_{\text{F}} (133 \text{ pm})$ , respectively [32,33]. Thus, the electrostatic repulsions between halogen anions and sample's surface are in the same order with their



**Scheme 1.** The process of molten salt synthetic approach for  $\text{CaCu}_3\text{Ti}_4\text{O}_{12}$ .

electronegativities. Considering such surface interactions between the catalysts and salts, we deduced that the ionized halogen ions i., F, could completely interact with the various surfaces/edges of  $\text{CaCu}_3\text{Ti}_4\text{O}_{12}$  to decrease surface energy to generate cubic structures with specific crystal facets. During the crystal growth process, the employed salt ions hardly incorporated in the structure since the ionic radius of introduced anions and K (138 pm) are larger than that of the cation radii of Ca (134 pm) [32,33]. Moreover, the stepwise ionization of molten salts could provide enough time for structure assembling and directly influence surface property and minimize surface energy to stabilize the crystal lattice, as a result, the assorted crystal shapes of  $\text{CaCu}_3\text{Ti}_4\text{O}_{12}$  are generated. Such dramatic variations in crystal shapes are ascribed to well-controlled synthetic procedures since the molten salt reaction follows a gradual ionization–nucleation–crystallization–recrystallization process (Scheme 1) [26–30].

### 3.1.2. Phase determination

As shown in Fig. 3, observed diffraction peaks are well matched with the cubic phase of  $\text{CaCu}_3\text{Ti}_4\text{O}_{12}$  (JCPDS card No. 75–2188,  $Im\bar{3}$  (204) space group,  $a = 7.39 \text{ \AA}$ ) and rule out the possibility of other peaks of impurities. The experimental powder XRD peak positions in as-obtained nanostructures are in good fit with the calculated one from its single crystal data, suggesting phase purities and single crystalline characters of fabricated  $\text{CaCu}_3\text{Ti}_4\text{O}_{12}$ , which are crystallized in cubic crystal system (Fig. 3, right). Compared to standard phase of  $\text{CaCu}_3\text{Ti}_4\text{O}_{12}$ , the relatively higher peak intensities e.g., (220) and (004) peaks in the patterns suggesting that high degree of crystallinity and more exposed facets were generated in samples during the molten salt synthesis.

### 3.2. Investigation of photocatalytic effectiveness

#### 3.2.1. Visible light degradation of antibiotic

Overuse and release of pharmaceutical residents such as antibiotics, have potential risks on human health as well as environment. According to the World Health Organization (WHO), release of antibiotics to the environment is causing antibiotics resistance bacteria and antibiotics resistant genes, a serious health issue of this century [34]. Among the various antibiotics used in human and veterinary to treat bacterial infection, tetracycline is extensively applied. Removal of tetracycline in the polluted water is urgently needed in order to protect human health and ecological systems. From this prospect and to understand the structure property correlations of  $\text{CaCu}_3\text{Ti}_4\text{O}_{12}$ , their photocatalytic activities were evaluated by antibiotic degradation under visible light irradiation.

To clarify the photoactivity of the as-obtained  $\text{CaCu}_3\text{Ti}_4\text{O}_{12}$  samples, series of blank experiments were carried out, e.g., in the absence of catalyst, light and  $\text{O}_2$  in the vacuum treated system. Blank experiments suggest that the tetracycline concentration could hardly be changed without light and catalyst, which further testify the significance of above parameters. The experimental results of the visible light-driven photocatalytic activity of as-obtained samples in decomposing antibiotic are depicted in Fig. 4a. It is found that corresponding degradation efficiencies increased in a certain extent upon prolonging the irritation time, demonstrating rapid disintegration of tetracycline in the presence of  $\text{CaCu}_3\text{Ti}_4\text{O}_{12}$  catalysts. The specific degradation percentages of tetracycline are obtained and analyzed according to the following equation [35]:

$$D(\%) = [(C_0 - C_t)/C_0] \times 100\%$$

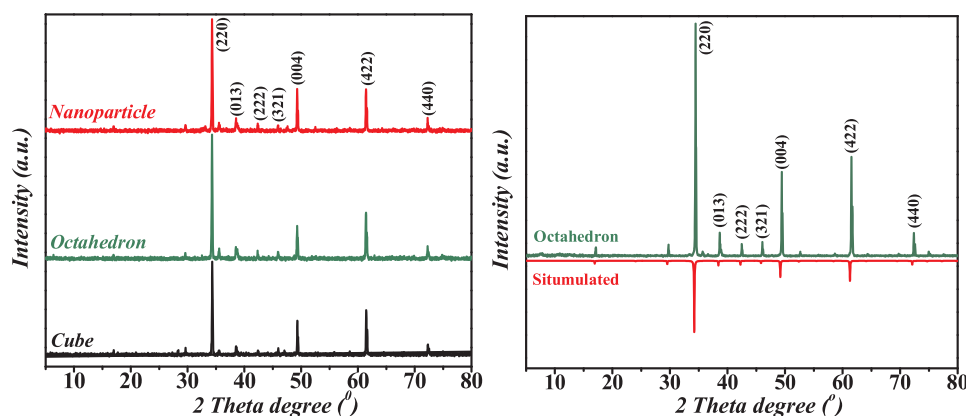


**Fig. 3.** XRD patterns of as-obtained  $\text{CaCu}_3\text{Ti}_4\text{O}_{12}$  catalysts: cube, octahedron and nanoparticle (left); Simulated and experimental XRD patterns of octahedron shaped  $\text{CaCu}_3\text{Ti}_4\text{O}_{12}$  (right).

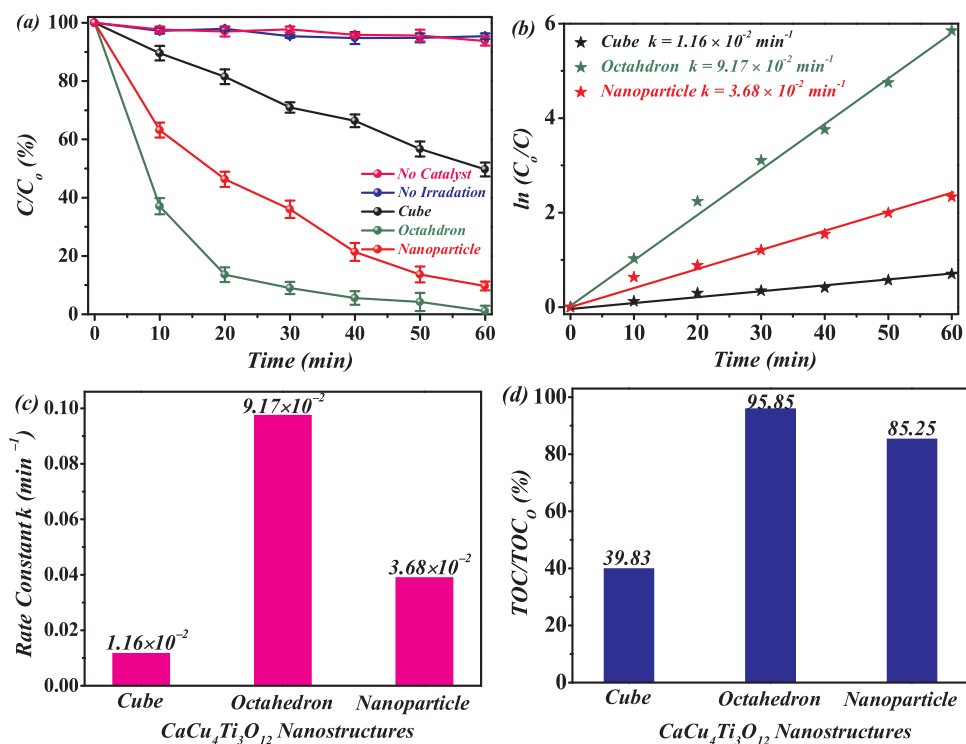


Fig. 4. (a) Comparison tetracycline degradation ratio over  $\text{CaCu}_3\text{Ti}_4\text{O}_{12}$  samples; (b) Plot of  $\ln(C_0/C)$  as a function of irradiation time of tetracycline decompositions and corresponding apparent rate constants; (c and d) Comparative apparent rate constants and total organic carbon (TOC) removal of tetracycline degradation over  $\text{CaCu}_3\text{Ti}_4\text{O}_{12}$ : Cube, Octahedron and Nanoparticle.

where  $C_0$  and  $C_t$  are tetracycline concentration at initial and after given irradiation time  $t$ . Nearly  $\sim 98.15\%$  tetracycline is removed in the presence of octahedron shaped  $\text{CaCu}_3\text{Ti}_4\text{O}_{12}$ . After 60 min degradation, the residual percentages of tetracycline aqueous solution over  $\text{CaCu}_3\text{Ti}_4\text{O}_{12}$  are in the following sequences: cube (49.69%) > nanoparticle (15.582%) > octahedron (1.851%), respectively (Fig. 4a).

### 3.2.2. Reaction kinetics

To quantify the reaction efficiency, the kinetics of the tetracycline decomposition is also investigated. The calculated results verify that  $\ln(C_0/C)$  of all studied samples show linear fit with the irradiation time, demonstrating that the decomposition obeys the rules of first-order kinetic model (Fig. 4b). The apparent rate constants of tetracycline decomposition were calculated according to the empirical equation of  $\ln(C_0/C) = kt$  [35]. The results show that the corresponding rate constants  $k$  ( $\text{min}^{-1}$ ) of tetracycline degradations are in the order of:  $0.0917 \text{ min}^{-1}$  (octahedrons) >  $0.0368 \text{ min}^{-1}$  (nanoparticles) >  $0.01165 \text{ min}^{-1}$  (cubes), respectively (Fig. 4c). It can be concluded through comparative analysis of the degradation efficiency and apparent reaction rates that the highest efficiency and fast decomposition was observed in octahedron shaped  $\text{CaCu}_3\text{Ti}_4\text{O}_{12}$  crystal, approximately 2.49 folds and 7.87 times faster than those of nanoparticle and cube under the same reaction conditions.

### 3.2.3. Photocatalytic efficiencies

Turn over number (TON) and turnover frequency (TOF) are significant parameters that can give more reliable quantitative results to evaluate innate photocatalytic activity of semiconductors [36,37]. TON is generally can be determined by the number of reacted molecules to that of an active site though it is obscure to calculated the number of reacted electrons since complex kinetics of the photodegradation reaction and decomposed products. Alternatively, comparison of initial TOF is more reasonable and it can provide intrinsic photocatalytic performances of catalysts. Specifically, TOF can be determined from the following equation [38]:

$$\text{TOF} = \frac{k \text{ (s}^{-1}\text{)} \times [\text{TC}]_{t=0} \text{ (M)}}{[\text{Cat.}] \text{ (M)}}$$

where  $k$  is the apparent rate constants ( $\text{s}^{-1}$ );  $[\text{TC}]_{t=0}$  and  $[\text{Cat.}]$  are the initial concentration of probe molecules and photocatalysts, respectively. Herein, corresponding calculated TOF for as-studied samples are  $0.298 \times 10^{-5} \text{ s}^{-1}$  (cube),  $2.35 \times 10^{-5} \text{ s}^{-1}$  (octahedron) and  $0.942 \times 10^{-5} \text{ s}^{-1}$  (nanoparticles), respectively. Same calculation method were employed for the assessment of photocatalytic activity of ZnO and  $\text{TiO}_2$ , and our results are quite consistent with the obtained TOF parameters in ZnO and  $\text{TiO}_2$  that within the range from  $10^{-6} \text{ s}^{-1}$  to  $10^{-2} \text{ s}^{-1}$  [38]. Evidently, it can be seen from the obtained TOF results that the intrinsic photocatalytic activities of as-obtained  $\text{CaCu}_3\text{Ti}_4\text{O}_{12}$  are in the order of octahedron > nanoparticle > cube, respectively.

### 3.2.4. Mineralization degree assessment

To assess the mineralization degree of tetracycline degradation, the total organic carbon (TOC) measurement was carried out as a mineralized index. The reduced TOC (%) was calculated based on the well-known equation [35]:

$$\text{TOC removal (\%)} = (\text{TOC}_0 - \text{TOC}_t) / \text{TOC}_0 \times 100\%$$

where  $\text{TOC}_0$  and  $\text{TOC}_t$  (ppm) are measured TOC values at initial and after given interval. Nearly 95.86% of reduced TOC is achieved over octahedron shaped  $\text{CaCu}_3\text{Ti}_4\text{O}_{12}$ , while its counterparts exhibit TOC residential concentrations of about 60.17% (cubes) and 14.75% (nanoparticles), respectively (Fig. 4d). The largest apparent rate constant, the highest degradation and relatively high TOC removal efficiency demonstrating the quick decomposition and complete mineralization of tetracycline with the assistance of octahedron shaped  $\text{CaCu}_3\text{Ti}_4\text{O}_{12}$ . Thus, it was selected for the following studies.

### 3.2.5. Catalyst reproducibility and stability

A retrievability and long-term stability are the important standards of efficient photocatalyst for its sustainable applications. To investigate the recyclable application and stability of octahedron shaped crystal, six runs successive degradation experiments were conducted. The experimental results show that every run of degradation gives high efficient visible light removal of tetracycline and no obvious decline is observed (Fig. 5a). After each reaction, the sample was collected and

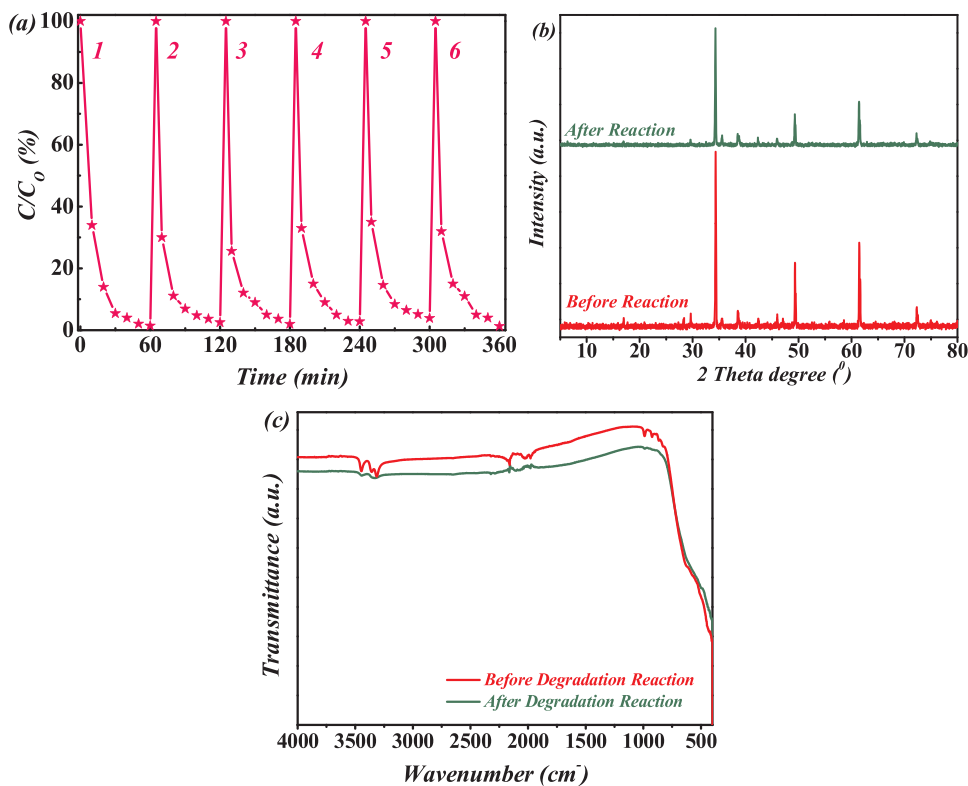


Fig. 5. (a) Six cycle degradations of tetracycline in the presence of octahedron shaped  $\text{CaCu}_3\text{Ti}_4\text{O}_{12}$ : catalyst shows high efficiency and stable photolysis even after 360 min visible light irradiation; (b and c) Comparative XRD and FTIR analyses of octahedron shaped  $\text{CaCu}_3\text{Ti}_4\text{O}_{12}$  before and after the decomposition experiments over octahedron shaped defective  $\text{CaCu}_3\text{Ti}_4\text{O}_{12}$ .

dried for further structure stability tests. The XRD patterns and FTIR spectra analyses before and after the six cycle successive decompositions are given in Fig. 5b and c. It can be found that unchanged peaks are observed in the XRD pattern except the peak intensity become weaker, implying that the chemical structures of studied photocatalysts are extremely robust. More importantly, no obvious exhaustion and photocorruption were take place even after 360 min continuous illumination with visible light as confirmed by unchanged FTIR vibrations. Overall, the octahedron shaped  $\text{CaCu}_3\text{Ti}_4\text{O}_{12}$  acquire high efficiency and outstanding stability, implying their potential applications as effective environmental catalysts for visible light degradation of pharmaceutical residues.

### 3.3. Mechanism of the improved photocatalytic decomposition

Why these  $\text{CaCu}_3\text{Ti}_4\text{O}_{12}$  samples have such great photocatalytic activities, especially the one with octahedron shapes? The diverse morphologies of  $\text{CaCu}_3\text{Ti}_4\text{O}_{12}$  play significant roles on photocatalytic activity, as arised from many factors such as strong visible light absorption, effective production/separation of photoinduced charge carriers, crystal deficiencies, surface areas as well as charge transfers as discussed below.

#### 3.3.1. Light absorption capability and energy band structure are major relevant

The solar light absorption properties of the cubes, octahedrons and nanoparticle of as-prepared  $\text{CaCu}_3\text{Ti}_4\text{O}_{12}$  were confirmed by UV-vis diffuse reflectance spectroscopy (DRS) measurements as depicted in Fig. 6. It can be found that the samples are typical visible light catalysts. The sample's electronic band gaps were analyzed according to the relation between the absorption coefficient ( $R$ ) and photon energy ( $h\nu$ ) can be described as  $(\alpha h\nu)^{1/2} = A(h\nu - E_g)$ , where  $A$  is absorption constants [39]. The optical band gaps of samples are estimated to be 2.661 eV (cube), 2.072 eV (octahedron) and 2.532 eV (nanoparticle), respectively. The abrupt change of light absorption spectrum and tailored wavelength at around 650 nm suggested that the optical band gap

of octahedron shaped sample was narrowed substantially. The narrow band gaps of  $\text{CaCu}_3\text{Ti}_4\text{O}_{12}$  samples are mainly due to the charge transformations from valence band to conduction band. Moreover, compared with widely studied famous star photocatalysts  $\text{TiO}_2$  ( $\sim 3.21$  eV) and  $\text{CaTiO}_3$  ( $\sim 3.76$  eV), whose valence bands are mostly composed of O 2p orbitals, the valence band of  $\text{CaCu}_3\text{Ti}_4\text{O}_{12}$  is comprised of the hybridized Cu 3d + O 2p states, which leads to its narrower band gap [40,41]. The observed strong and broad light absorption between 360 nm–400 nm can be assigned to the electron excitation from  $\text{TiO}_6$  units, while the absorption peaks from 450 nm–600 nm are ascribed to the electron transition from the hybridized Cu 3d – O 2p valence band to the unoccupied Ti 3d composed conduction band. The captured strong absorptions are arised from their unique structure of nanoscale morphologies, whereas the broad tailored absorptions from 450 nm to 650 nm are ascribed to defects, i., crystal disorder in  $\text{TiO}_6$  and  $\text{TiO}_5\text{Vo}$  clusters (Vo representing oxygen deficiency). Therefore, crystal structures and electronic band configurations determined the band gap energy of studied samples, which in turn directly influence their light absorptions. Importantly, these defects are associated with electronic band gap of materials and, to some extent, are the electron or hole trapping centers to promote charge carrier separation.

#### 3.3.2. Effective production of electron-hole pairs are primarily significant

In the photocatalytic reaction, after excitation of  $\text{CaCu}_3\text{Ti}_4\text{O}_{12}$  with visible light, conduction band electrons and valence band holes are generated. These photoinduced electron-hole pairs will invoke further photocatalytic reactions. Therefore, effective production of carriers is the precondition to exert a photoreaction. Meanwhile, photocatalysts with appropriate redox potentials can fulfil the photocatalytic solar energy conversion. To clarify the process of efficient photolysis, the sample's band structures were analyzed first. Theoretically, the band edge positions are determined from the following equations [32,34]:

$$E_{\text{CB}} = \chi - E_{\text{c}} - 0.5 E_{\text{g}} \text{ and } E_{\text{VB}} = E_{\text{g}} + E_{\text{CB}}$$

where  $E_{\text{CB}}$  and  $E_{\text{VB}}$  are the conduction band and valence band positions,  $\chi$  is an electronegativity of the catalysts, estimated from the absolute

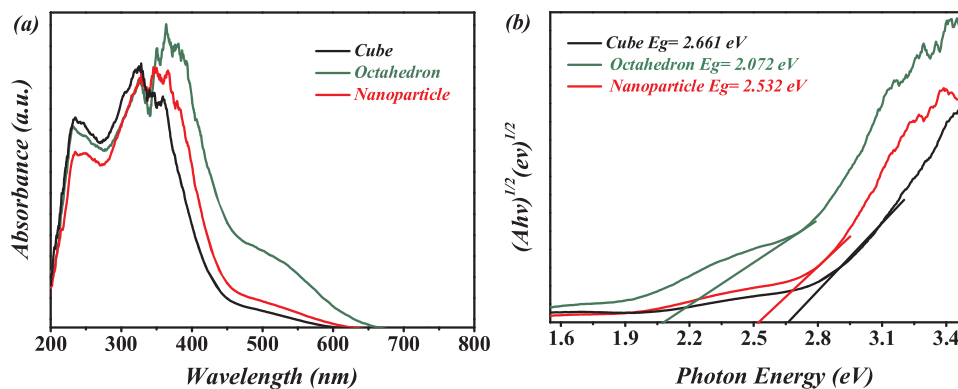


Fig. 6. (a) Room-temperature UV-vis absorption spectra of  $\text{CaCu}_3\text{Ti}_4\text{O}_{12}$  shapes of cube, octahedron, nanoparticle and, (b) The corresponding photon energy hv.

Table 1

Synthesis, morphology and optical property of  $\text{CaCu}_3\text{Ti}_4\text{O}_{12}$ .

Salt system	Melting point (°C)	Morphology	Band gap (eV)	Band edge positions (eV)	
				Conduction band	Valence band
KF	770	Cube	2.661	-0.226	2.4384
KCl	776	Octahedron	2.072	0.0719	2.1439
KBr	734	Nanoparticle	2.532	-0.158	2.3739

electronegativity of comprised elements  $\chi = (\chi_A^a \chi_B^b \chi_C^c)^{1/(a+b+c)}$ ,  $E_C$  is a constant scale factor taken as  $-4.5$  eV, and  $E_g$  is the electronic band gap of semiconductors. The valence band edges of prepared samples are determined to be  $2.438$  eV (cube),  $2.144$  eV (octahedron) and  $2.374$  eV (nanoparticle), while their corresponding conduction band positions are estimated to be  $-0.226$  eV,  $0.0719$  eV and  $-0.158$  eV, respectively. The Table 1 summarizes the detailed reaction conditions and properties of as-obtained catalysts.

Calculated band edge positions indicating the effective formation of superoxide radicals ( $\cdot\text{O}_2^-$ ) in cubes and nanoparticles is quite reasonable since their conduction band potentials ( $-0.226$  eV and  $-0.158$  eV, respectively) are located right above the potentials of  $\text{O}_2/\cdot\text{O}_2^-$  ( $-0.046$  eV vs. NHE) at pH = 7.0 [42]. Meanwhile, the valence band positions of  $\text{CaCu}_3\text{Ti}_4\text{O}_{12}$  are more positive than  $\cdot\text{OH}/\text{OH}^-$  ( $1.99$  eV vs. NHE) species, favorable to formation of active radicals of  $\cdot\text{OH}$  and  $\text{OH}^-$ . Interestingly, as-obtained cubes possess the most suitable band edge positions though exhibit relatively lower degradation efficiency. From the crystallography point of view, as-obtained cubes predominant with (001) and (110) exposed crystal facets, on which five-coordinated unsaturated Ti cations are exist (Fig. 7). This unsaturated surface atomic coordination could provide active sites for the adsorptions of oxygen molecules, water and pollutants etc., thus as-obtained cubes display certain decomposition efficiency.

Thermodynamically, the redox potentials of octahedron shaped  $\text{CaCu}_3\text{Ti}_4\text{O}_{12}$  ( $E_{CB} = 0.0719$  eV) implying that the superoxide radicals are hardly generated during the photolysis. However, it can be speculated from its redox potentials that the electron transfer pathway may relevant for the generations of more active radicals such as  $\text{O}_2$ , hydrogen peroxide ( $\text{H}_2\text{O}_2$ ) or  $\cdot\text{OH}$  with visible light irradiation as the conduction band potential of sample is relatively negative than that of the potential of  $\text{O}_2/\text{H}_2\text{O}_2$  [43]. Compare to as-obtained nanoparticles and cubes, narrower band gap of octahedron shaped crystal makes it relatively easier to be excited with visible light irradiation, thus more electrons are generated. These conduction band electrons could directly reduce  $\text{O}_2$  to produce  $\text{H}_2\text{O}_2$  species, which would further disintegrate the tetracycline molecule. The effective generation of  $\text{H}_2\text{O}_2$  as well as its influential factors will be introduced in our further work soon. On the other hand, the electrons transferred between metals ( $\text{Ti}^{4+}$  and

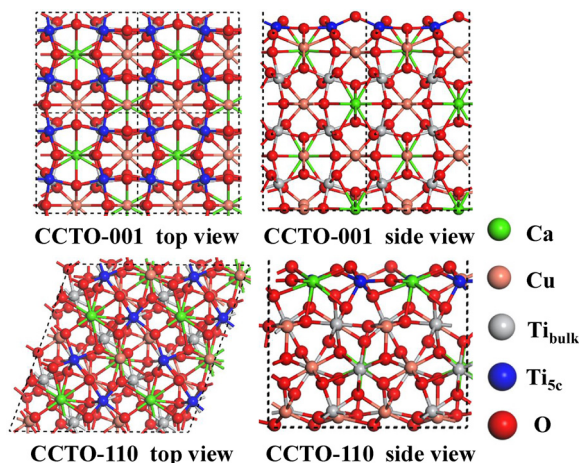


Fig. 7. Five coordinated Ti atoms on the (001) and (110) crystal facets act as active reaction sites.

$\text{Cu}^{2+}$ ) can generate  $\cdot\text{O}_2^-$  radicals via react with surface adsorbed oxygen to further facilitate the carrier separation and give rise to efficiency enhancement. As the case of as-obtained small nanoparticles, relatively appropriate redox potentials leading to carrier separation, thus give relatively higher efficiency (84.42%). Therefore, it can be assumed from above discussions that assorted band edge positions of  $\text{CaCu}_3\text{Ti}_4\text{O}_{12}$  catalysts indicating effective production of photocatalytically active species (will be discussed in the following section), which give rise to superior redox capabilities (Fig. 8).

### 3.3.3. Crystal defects are significantly crucial for enhanced visible light photolysis

$\text{CaCu}_3\text{Ti}_4\text{O}_{12}$  is very different from other perovskites, especially from those of ferroelectric perovskites [44]. The optical and conduction properties of  $\text{CaCu}_3\text{Ti}_4\text{O}_{12}$  are influenced by crystal defects, while features of the ferroelectrics are strongly related to their non-centrosymmetrical structure. Theoretical investigations on the structure performance correlations revealed that oxygen vacancies were generated easily for charge balance in the  $\text{CaCu}_3\text{Ti}_4\text{O}_{12}$  and were crucial for efficiency enhancement [21]. In the case of  $\text{CaCu}_3\text{Ti}_4\text{O}_{12}$  catalysts prepared via molten salt reaction, the stepwise ionizations of employed salts contribute to the distributions of oxygen vacant sites. Existence of crystal defects in the structure not only act as active reaction sites to increase surface adsorption of reactants and molecule oxygen activation, but accelerate effective production of stronger oxidant such as superoxide radicals ( $\text{O}_2^{\cdot-}$ ) since they are also the carrier/electron trapping centres that can mitigate carrier recombination rates during the reaction. More reliable information on the defects is obtained from electron paramagnetic resonance (EPR) measurements. The observed

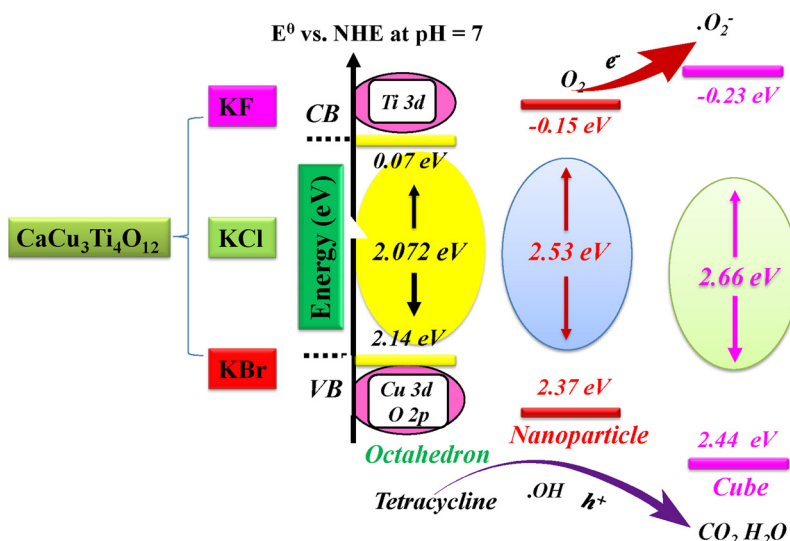


Fig. 8. The determined band edges and visible light degradation mechanism of tetracycline over assorted morphological  $\text{CaCu}_3\text{Ti}_4\text{O}_{12}$  photocatalysts.

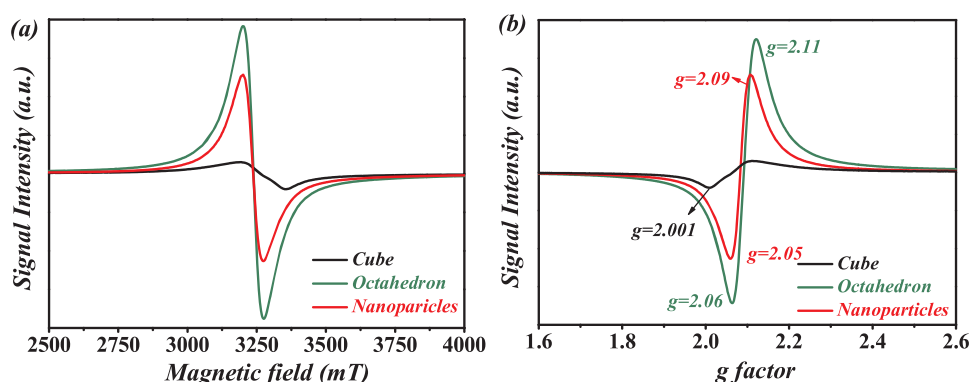


Fig. 9. EPR spectra and the corresponding g factors obtained from EPR signals of  $\text{CaCu}_3\text{Ti}_4\text{O}_{12}$ .

EPR signals show different intensities at around the g values of 2.00–2.50, which can be attributed to the copper oxygen vacancy in  $\text{CaCu}_3\text{Ti}_4\text{O}_{12}$  photocatalysts (Fig. 9a) [45]. As shown in Fig. 9b, narrow EPR signals with relatively strong intensities are observed in the octahedrons and nanoparticles with the g value of about 2.06–2.11, demonstrating the existence of oxygen vacancy in the structure, which are quite consistent with strong optical absorptions as observed DRS results (Fig. 6).

Surprisingly, the broad and weak representative EPR signals are captured in the cube shaped  $\text{CaCu}_3\text{Ti}_4\text{O}_{12}$  with the g value of  $\sim 2.001$ , indicating existence of certain amounts of  $\text{Ti}^{3+}$  species in the structure. From the structure point of view, in the  $\text{CaCu}_3\text{Ti}_4\text{O}_{12}$  catalysts, missing of any oxygen atoms in  $\text{TiO}_6$  framework or  $\text{CuO}_4$  unit leading to surface variations, charge distributions, even the distortion and consequently the internal field changes. Thus, the stronger the distortion degree, the higher the defects in the structure. For instance, the distortion of  $\text{TiO}_6$  clusters in octahedrons are greater than that of distortions in cubes or nanoparticles. Moreover, the electron transformation of  $\text{Cu}^{2+} + \text{e}^- \rightarrow \text{Cu}^+$ ,  $\text{Ti}^{4+} + \text{e}^- \rightarrow \text{Ti}^{3+}$  require opposite species such as, oxygen vacancy  $\text{O}^{2-}$  for charge balance. As a result, the plane defects are formed in  $\text{CuO}_4$  units, and will in turn resulting slightly distorted  $\text{TiO}_5$  clusters, which are mostly with  $\text{Ti}^{4+}$  and  $\text{Ti}^{3+}$ . Interactions of surface  $\text{Ti}^{3+}$  with adsorbed  $\text{O}_2$  molecules would generate high abundant surface oxygen vacancy  $\text{O}^-$ , of which the corresponding representative EPR signals are observed at around the g value of 2.001 [18]. Thus, it is reasonable to speculated that trace amounts of  $\text{Ti}^{3+}$  are formed during the reaction, then subsequently diffused into the cubes to generate surface oxygen

defects and react with surface adsorbed  $\text{O}_2$  molecules to produce more stronger oxidant superoxide anions  $\cdot\text{O}_2^-$  ( $\text{Ti}^{3+} + \text{O}_2 \rightarrow \text{Ti}^{4+} + \cdot\text{O}_2^-$ ). This is why the cube shaped crystals display certain photocatalytic efficiency for pollutant degradation.

It should be pointed out that the order-disorder lattice is significance for the optical property and charge transportations that arisen from unique body-centered cubic structure of  $\text{CaCu}_3\text{Ti}_4\text{O}_{12}$ . As discussed, the Ti atoms located in the B positions which are coordinated with six O atoms to form  $\text{TiO}_6$  clusters, while Cu atoms are connected with four O atoms which generate  $\text{CuO}_4$  units. These  $[\text{CuO}_4]$  and  $[\text{TiO}_6]$  clusters are linked to each other with Ti–O–Ti angles of about  $141^\circ$  (Fig. 10a). In other words, the positions of oxygen atoms in both units control the bond angles, charge states and atom arrangements in the unit cell. For instance, variations of the Cu–O bond length in the  $\text{CuO}_4$  cluster directly affect the distortion/tilting degree of  $\text{TiO}_6$  by changing  $[\text{TiO}_6]$  and  $[\text{TiO}_5\text{V}_\text{O}]$  in the structure (Fig. 10b). The perfect coordinations of  $\text{TiO}_6$  are the octahedron shapes, but can become tetrahedron and pyramidal when the plane defects of  $\text{CuO}_4$  are higher. Thus, with increasing of  $\text{V}_\text{O}$ , surface defects of metal deficiencies such as  $\text{Cu}^+$  from the  $[\text{CuO}_4]'$ ,  $[\text{CuO}_4]''$  units or  $\text{Ti}^{3+}$  species from the  $[\text{TiO}_5\text{V}_\text{O}]'$ ,  $[\text{TiO}_5\text{V}_\text{O}]''$  clusters are generated. Actually, presence of oxygen vacancy and  $\text{Cu}^+$  will decrease electron mobility while the  $\text{Ti}^{3+}$  give significant enhancement in carrier mobility [10]. Moreover, the  $\text{Ti}^{3+}$  species can disrupt Ti–O bonds in  $\text{TiO}_6$  cluster resulting in local electrical polarization. In this way, the distortions of  $\text{TiO}_6$  ( $\text{TiO}_5\text{V}_\text{O}$ ) clusters can facilitate electron transformation between  $\text{Ti}^{3+}$  and  $\text{Ti}^{4+}$ . Besides, the charge transformation from  $[\text{TiO}_5\text{V}_\text{O}]'$  to  $[\text{CuO}_4]'$  can improve

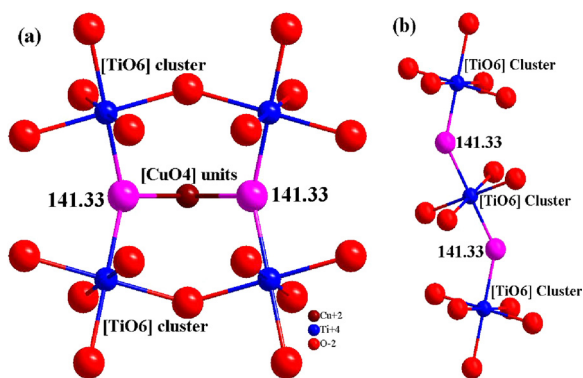
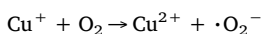
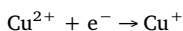
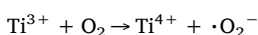
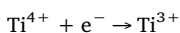


**Fig. 10.** (a) Two  $[\text{TiO}_6]$  clusters linked each other with O atoms from  $\text{CuO}_4$  units; (b) Distortion of  $[\text{TiO}_6]$  units in  $\text{CaCu}_3\text{Ti}_4\text{O}_{12}$ .

conductivity and provide chance for  $\text{Ti}^{3+}$  and  $\text{Cu}^+$  species generation.

Importantly, oxygen deficiencies can bind oxygen molecules and the concentration of bulk oxygen defects is decreases, resulting in oxidation of acceptor defects ( $\text{Cu}^+$  and  $\text{Ti}^{3+}$ ). Thus, oxygen defects act as electron scavenger to generate superoxide radicals ( $\cdot\text{O}_2^-$ ) as a result of effective charge transportation from vacant sites to oxygen molecules:



In the  $n$  type of photocatalysts, i.e.,  $\text{CaCu}_3\text{Ti}_4\text{O}_{12}$ , oxygen defects are mostly negatively charged and compensated by oppositely charged carriers, thus resulting in improved carrier mobility [45]. Additionally, these defects not only are act as  $\text{O}_2$  binding sites to generate more  $\text{O}^-$  species, but can become active sites to accelerate the reactant (i., water, pollutant and oxygen molecule) adsorption and promote carrier migration to the catalyst's surface or directly involve in the photocatalytic reactions and contribute to the enhanced photocatalytic efficiency. Herein, the presence of defects significantly affect the sample's light absorption edges from 2.66 eV (cube), 2.53 eV (nanoparticle) to 2.07 eV (octahedron). Extended light absorptions from 465.9 nm to 598.5 nm were ascribed to the formation of disorder-induced mid-band tail states as a result of occupation of oxygen deficiencies by unpaired electrons, consistence with the EPR results. Indeed, detected oxygen deficiency concentrations are quite different in the order of: octahedron > nanoparticle > cube (Fig. 11), all in good agreement with the sequences of degradation efficiencies. It can be assumed from the above analyses that octahedron shaped crystal holds the highest amounts of deficiencies, quite consistent with EPR results (Fig. 9a).

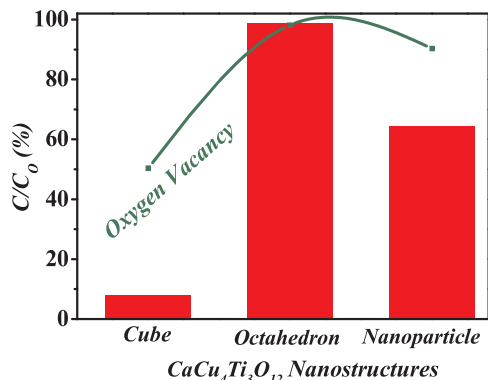


**Fig. 11.** Correlations between oxygen deficiency and photocatalytic performance of  $\text{CaCu}_3\text{Ti}_4\text{O}_{12}$ .

### 3.3.4. Surface area and carrier separation are relevant for improved photocatalytic efficiency

The surface area is one of the significant parameters for improving photocatalytic activity. The samples surface areas were determined to be  $3.386 \text{ m}^2 \text{ g}^{-1}$  (cube),  $7.273 \text{ m}^2 \text{ g}^{-1}$  (octahedron) and  $10.12 \text{ m}^2 \text{ g}^{-1}$  (nanoparticle), respectively (Fig. 12a). Obviously, the nanoparticles acquire the highest surface area among samples, thus, it was expected to hold more active reaction sites and display better photocatalytic activity. Oppositely, as-prepared nanoparticles exhibit second higher photocatalytic performance with 84.41% degradation, while the highest decomposition efficiency (98.15%) is observed in octahedron shaped  $\text{CaCu}_3\text{Ti}_4\text{O}_{12}$  (BET  $\sim 7.273 \text{ m}^2 \text{ g}^{-1}$ ), implying that there is no correlation between the photocatalytic efficiency and surface areas. However, as-obtained  $\text{CaCu}_3\text{Ti}_4\text{O}_{12}$  nanostructures give surprising results on photocatalytic decompositions when the reaction rate constants are normalized to their surface areas. The cubes and nanoparticles acquire quite different surface areas ( $3.386 \text{ m}^2 \text{ g}^{-1}$  and  $10.12 \text{ m}^2 \text{ g}^{-1}$ , respectively) though display similar degradation performances of about  $3.425 \times 10^{-3} \text{ g min}^{-1} \text{ m}^{-2}$  and  $3.636 \times 10^{-3} \text{ g min}^{-1} \text{ m}^{-2}$  when the rate constants are normalized to the degradation results. The normalized rate constant for octahedron shaped crystal is  $1.261 \times 10^{-2} \text{ g min}^{-1} \text{ m}^{-2}$ , nearly 3.687 and 3.474 folds higher than its counterparts, cubes and nanoparticles. It can be concluded from above comparative results that octahedron shaped  $\text{CaCu}_3\text{Ti}_4\text{O}_{12}$  exhibit the highest degradation performance among studied samples. Significantly, the normalized oxygen vacancy concentrations are in good agreement with those sequences of degradation efficiencies as follow the order of: octahedron > nanoparticle > cube (inset in the Fig. 12a). Therefore, it can be concluded that the more important factor that governs tetracycline degradation activity is oxygen deficiency rather than the surface areas.

During the degradation process, photoinduced electron–holes have chance to recombine together and decrease the reaction efficiency. From the structure point of view, in  $\text{CaCu}_3\text{Ti}_4\text{O}_{12}$ , the charge transfer between metal ions ( $\text{Ti}^{4+} + \text{Cu}^{2+} \rightarrow \text{Ti}^{3+} + \text{Cu}^{3+}$ ) occupied distinct crystallographic sublattices to generate photoactive electrons, which would transfer from conduction band to valence band. The photo-induced electrons react with surface adsorbed oxygen to contributing electron–hole separation. The effective electron–hole pairs separation in semiconductors can be understood by comparing their photocurrent responses. As can be seen from photocurrent-time curves in Fig. 12b that the samples give different photocurrent intensity under visible light irradiating and in the absence of light. Significantly, Octahedron exhibits relatively higher photocurrent response. It is well-known that the higher the photocurrent responses the higher the carrier separations. Therefore, electron-hole recombination rates of samples are in the order of: Cube > Nanoparticle > Octahedron, respectively. Therefore, with the efficient electron transfer between metals and high amounts of oxygen vacancies, the recombination of charge carriers can be prevented, which is favorable to enhance photocatalytic degradation of tetracycline under visible light. Thus, it can be concluded that high performance effectiveness of tetracycline decomposition over defective  $\text{CaCu}_3\text{Ti}_4\text{O}_{12}$  samples can be attributed to the surface defects and effective carrier separations. The surface properties and photocatalytic efficiencies of tetracycline degradation in the presence of  $\text{CaCu}_3\text{Ti}_4\text{O}_{12}$  samples are listed in Table 2.

### 3.3.5. Active Radicals play pivotal roles on pronounced photocatalytic effectiveness

The commonly related photocatalytically radicals i., hydroxyl radicals ( $\cdot\text{OH}$ ), superoxide anions ( $\cdot\text{O}_2^-$ ), holes ( $h^+$ ) and electrons ( $e^-$ ) are concerned in the efficiency enhancement. The quantitative radical trapping tests were carried out to confirmed involved active species in tetracycline degradation, in which various scavengers of  $P$ -benzoquinone (BQ), isopropyl (IPA), silver nitrate ( $\text{AgNO}_3$ ) and ammonium oxalate (AO) were applied as  $\cdot\text{O}_2^-$ ,  $\cdot\text{OH}$ ,  $e^-$  and  $h^+$

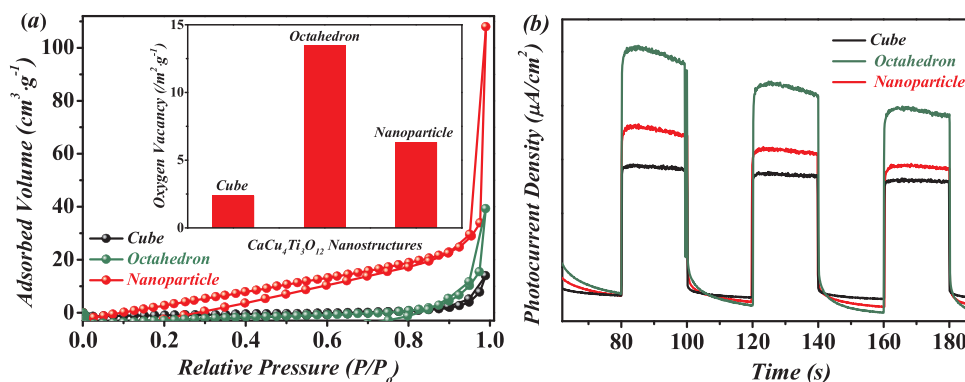


**Fig. 12.** (a) Nitrogen adsorption–desorption isotherms of defective  $\text{CaCu}_3\text{Ti}_4\text{O}_{12}$  nanostructures. Inset: Normalized oxygen vacancy percentages on defective  $\text{CaCu}_3\text{Ti}_4\text{O}_{12}$  samples; (b) photocurrents of defective  $\text{CaCu}_3\text{Ti}_4\text{O}_{12}$  nanostructure of cubes, octahedrons and nanoparticles.

**Table 2**

Surface property and visible light photocatalytic activity of  $\text{CaCu}_3\text{Ti}_4\text{O}_{12}$  samples.

Morphology	Surface area ( $\text{m}^2 \text{g}^{-1}$ )	Tetracycline degradation (%)	TOC removal (%)	First-order rate constant $k$ ( $\text{min}^{-1}$ )	Normalized $k$ ( $\text{g min}^{-1} \text{m}^{-2}$ )
Cube	3.386	50.31	39.83	$1.165 \times 10^{-2}$	$3.425 \times 10^{-3}$
Octahedron	7.273	98.15	95.86	$9.172 \times 10^{-2}$	$1.261 \times 10^{-2}$
Nanoparticle	10.12	84.42	85.25	$3.684 \times 10^{-2}$	$3.636 \times 10^{-3}$

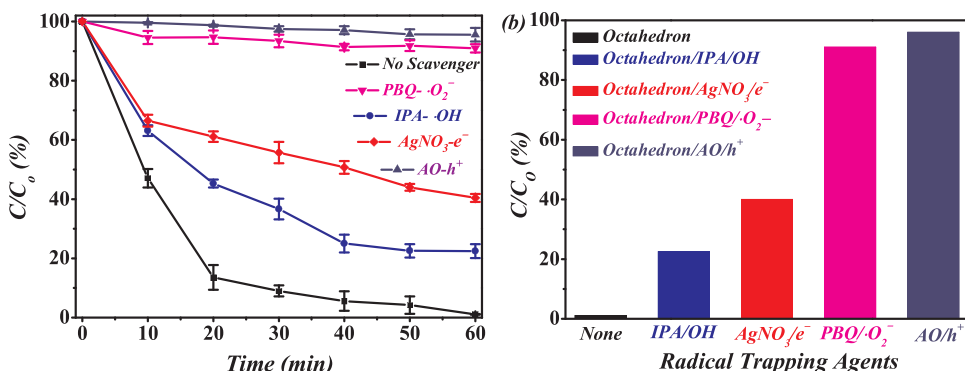


**Fig. 13.** (a) Trapping experiments of active species and (b) Comparison results of influences of various scavengers for tetracycline degradation in the presence of octahedron shaped  $\text{CaCu}_3\text{Ti}_4\text{O}_{12}$ . IPA: Isopropyl alcohol, as a hydroxide ( $\cdot\text{OH}$ ) scavenger; AO: Ammonium oxalate was introduced as hole ( $h^+$ ) trapping agents; PBQ: *P*-benzoquinone was used as a superoxide ( $\cdot\text{O}_2^-$ ) scavenger;  $\text{AgNO}_3$  was selected as an electron ( $e^-$ ) scavenger, respectively.

trapping agents, respectively. The tetracycline decomposition was significantly hampered when PBQ and AO introduced into the solution, and the degradation decreased slightly when  $\text{AgNO}_3$  was added (Fig. 13a). Interestingly, no obvious decline seen with the addition of IPA as  $\cdot\text{OH}$  scavenger. The  $e^-$  has contribution to some extent, and the  $\cdot\text{OH}$  radical has minor effort for antibiotic degradation over  $\text{CaCu}_3\text{Ti}_4\text{O}_{12}$ . As can be summarized from the comparison results that the  $\cdot\text{O}_2^-$  and  $h^+$  playing utmost role and these should be the two important active radicals for tetracycline degradation as depicted in Fig. 13b.

In order to make clear for involved active species, the EPR spin trapping experiments were also conducted. After 5 min visible light irradiation, the sextet strong characteristic peaks of  $\cdot\text{O}_2^-$  radicals are detected with the addition of the 5, 5-dimethyl-1-pyrroline *N*-oxide (DMPO) (Fig. 14a). Four-line ESR signals of 1:2:2:1 were captured with the addition of DMPO as  $\cdot\text{OH}$  spin trapper as shown in Fig. 14b, implying that the  $\cdot\text{OH}$  radicals were generated and, to some extent, contributed to the tetracycline oxidation. These results are agree well with redox potentials of octahedron shaped sample and quantitative radical capturing experiments. For detection of photoinduced electrons, the 2, 2, 6, 6-tetramethylpiperidine-1-oxyl (TEMPO) was introduced into the reaction. No obvious peaks were detected with the absence of light irradiation, giving clear evidence that the electrons are generated only with light irradiation. With increasing of irradiation time, the predominant triplet representative peaks with the intensity of about

1:1:1 of TEMPO- $e^-$  were captured and the corresponding ESR signals of electrons monitored are exhibited in Fig. 14c. Finally, the 1-hydroxy-3-carboxy-2, 2, 5, 5-tetramethylpyrrolidine (CPH) was applied for detection of photoinduced holes, in which very strong, triplet characteristic ESR signals of  $h^+$  are captured as exhibited in Fig. 14d. Overall, above results give the clear evidence that an important parameters play significant role in efficiency enhancement is suitable band edge positions, defects and photocatalytically active radicals ( $e^-$ ,  $\cdot\text{O}_2^-$  and  $h^+$ ). With the assistance of aforementioned factors and defective  $\text{CaCu}_3\text{Ti}_4\text{O}_{12}$  perovskite, the antibiotic molecule mineralized eventually into small fragments.

#### 4. Conclusions

In summary, the structure-property relationship of newly explored, visible light active perovskite  $\text{CaCu}_3\text{Ti}_4\text{O}_{12}$  is systematically studied as potential environmental photofunctional material. The following merits are worth highlighting:

- A time-saving, one-step, cost-effective and feasible molten salt reaction approach was developed to prepare various morphological perovskite  $\text{CaCu}_3\text{Ti}_4\text{O}_{12}$  with high yields of products merely through adjusting the halide anions of selected molten salts KX (X = F, Cl and Br) without introducing other shaped controlled agents. The detailed formation mechanisms of assorted structures

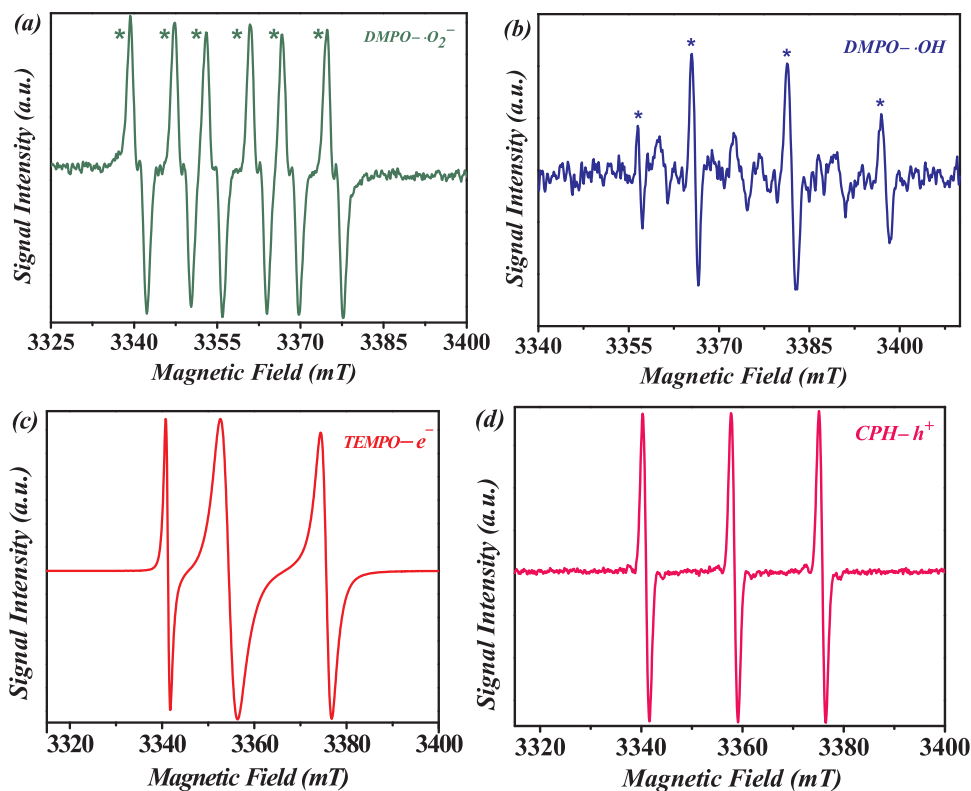


**Fig. 14.** (a and b) ESR detection of superoxide and hydroxyl radicals using a DMPO spin-trapping agent. The methanol/water solution of DMPO was preirradiated with octahedron shaped  $\text{CaCu}_3\text{Ti}_4\text{O}_{12}$ ; (c) ESR detection of photoinduced electrons with a TEMPO spin-trapping agent in the presence of octahedron shaped  $\text{CaCu}_3\text{Ti}_4\text{O}_{12}$ ; (d) ESR detection of photoinduced holes with a CPH spin-trapping agent over octahedron shaped  $\text{CaCu}_3\text{Ti}_4\text{O}_{12}$ .

- were well elaborated on the basis of physical and chemical characters of selected halide anions;
- (ii) This systematic study highlights that the structure and morphology of  $\text{CaCu}_3\text{Ti}_4\text{O}_{12}$  nanomaterials could be controllable via specifically vary the salt composition of flux agents, and thus their optical and electronic functions as well as photocatalytic properties are tuneable. Regulated morphology evolution and defect tuning merely with trace amounts of salt may open a new route towards rational design and synthesis of highly efficient, stable and visible light driven perovskite photocatalysts by providing a simple, green and economical technique for environmental remediation applications.
- (iii) Owing to strong visible light absorption, unique morphologies (cube, nanoparticle and octahedron) and oxygen deficiencies,  $\text{CaCu}_3\text{Ti}_4\text{O}_{12}$  display efficient photooxidation of antibiotic. The structure-performance relationships confirmed that these observed oxygen deficiencies play decisive roles in adjusting the optical band gap (light absorption) and enhancing efficiency (reaction kinetics) as a result of providing more active reaction sites and facilitating carrier separation during the photolysis. The scavenger and spin trapping investigations support that the photoinduced holes, electrons and superoxide radicals play synergetic roles in the degradation process.
- (iv) The high-performance of  $\text{CaCu}_3\text{Ti}_4\text{O}_{12}$  in tetracycline decomposition is attributed to its suitable band edge position, unique morphology, oxygen vacancy, effective charge transfer in the local structure and photocatalytically active radicals. Effective morphology tailoring, energy band gap and defect engineering in photocatalysts provide new inspirations on exploring new functionality of visible-light active materials by revealing structure-performance relationships and the corresponding reaction mechanisms.

Further investigations on the photocatalytic application of the well defined  $\text{CaCu}_3\text{Ti}_4\text{O}_{12}$  nanostructures such as detection of active species ( $\text{H}_2\text{O}_2$  generation), photoreduction of carbon dioxide and hydrogen evolution from water splitting may plausible.

## Acknowledgements

The authors are grateful to the financial support of the NSFC (Grant No. 21473248) and the CAS/SAFEA International Partnership Program for Creative Research Teams.

## References

- [1] M.R. Hoffmann, S.T. Martin, W. Choi, D.W. Bahnemann, *Chem. Rev.* 95 (1995) 69–96.
- [2] W. Wang, M.O. Tade, Z.P. Shao, *Chem. Soc. Rev.* 44 (2015) 5371–5408.
- [3] D.J. Martin, G.G. Liu, S.J.A. Moniz, Y.P. Bi, A.M. Beale, J.H. Ye, J.W. Tang, *Chem. Soc. Rev.* 44 (2015) 7808–7828.
- [4] A. Fujishima, K. Honda, *Nature* 238 (1972) 37–38.
- [5] X.B. Chen, L. Liu, P.Y. Yu, S.S. Mao, *Science* 331 (2011) 746–749.
- [6] Y.F. Ji, Y. Luo, *J. Am. Chem. Soc.* 138 (2016) 15896–15902.
- [7] H. Li, F. Qin, Z.P. Yang, X.M. Cui, J.F. Wang, L.Z. Zhang, *J. Am. Chem. Soc.* 139 (2017) 3513–3521.
- [8] Y.H. Lv, C.S. Pan, X.G. Ma, R.L. Zong, X.J. Bai, Y.F. Zhu, *Appl. Catal. B* 138 (2013) 26–32.
- [9] N. Zhang, X.Y. Li, H.C. Ye, S.M. Chen, H.X. Ju, D.B. Liu, Y. Lin, W. Ye, C.M. Wang, Q. Xu, F.F. Zhu, L. Song, J. Jiang, Y.J. Xiong, *J. Am. Chem. Soc.* 138 (2016) 8928–8935.
- [10] J.H. Clark, M.S. Dyer, R.G. Palgrave, C.P. Ireland, J.R. Darwent, M.J. Rosseinsky, *J. Am. Chem. Soc.* 133 (2011) 1016–1032.
- [11] H.S. Kushwaha, N.A. Madhar, B. Ilahi, P. Thomas, A. Halder, R. Vaish, *Sci. Rep.* 6 (2016) 18557–18657.
- [12] R. Hailili, Z.-Q. Wang, Y.X. Li, Y.H. Wang, K.S. Virender, X.-Q. Gong, C.Y. Wang, *Appl. Catal. B* 221 (2018) 422–432.
- [13] A. Sen, K.K. Chattopadhyay, *J. Mater. Sci.* 27 (2016) 10393–10398.
- [14] H.S. Kushwaha, P. Thomas, R. Vaish, *RSC Adv.* 5 (2015) 87241–87250.
- [15] H.G. Kim, O.S. Becker, J.S. Jang, S.M. Ji, P.H. Borse, J.S. Lee, *J. Solid State Chem.* 179 (2006) 1214–1218.
- [16] M.-H. Whangbo, M.A. Subramanian, *Chem. Mater.* 18 (2006) 3257–3260.
- [17] H. Zhang, J.M. Cai, Y.T. Wang, M.Q. Wu, M. Meng, Y. Tian, X.G. Li, J. Zhang, L.R. Zheng, Z. Jiang, J.L. Gong, *Appl. Catal. B* 220 (2018) 126–136.
- [18] S.F. Shao, J.L. Zhang, P. Zheng, W.L. Zhong, C.L. Wang, *J. Appl. Phys.* 99 (2006) 084106–084111.
- [19] W.X. Yuana, S.K. Harka, W.N. Meib, *J. Ceram. Process. Res.* 10 (2009) 696–699.
- [20] Y. Li, P. Liang, X. Chao, Z. Yang, *Ceram. Int.* 39 (2013) 7879–7889.
- [21] N. Wongpisutpaisan, N. Vittayakorn, A. Ruangphanit, W. Pecharapa, *Integr. Ferroelectr.* 149 (2013) 56–60.
- [22] Y.X. Li, S. Chen, H.Q. He, Y. Zhang, C.Y. Wang, *ACS Appl. Mater. Interfaces* 5 (2013) 10260–10265.

- [23] H.Q. He, J. Yin, Y.X. Li, Y. Zhang, H.S. Qiu, J.B. Xu, T. Xu, C.Y. Wang, *Appl. Catal. B* 156 (2014) 35–43.
- [24] Y.X. Li, B.R. Bunes, L. Zang, J. Zhao, Y. Li, Y.Q. Zhu, C.Y. Wang, *ACS Nano* 10 (2016) 2386–2391.
- [25] R. Hailili, G.H. Dong, S. Jin, C.Y. Wang, T. Xu, *Ind. Eng. Chem. Res.* 56 (2017) 2908–2916.
- [26] R. Hailili, Z.-Q. Wang, X.-Q. Gong, C.Y. Wang. Unpublished Results.
- [27] R. Hailili, C.Y. Wang. Unpublished Results.
- [28] W.W. He, H.-K. Kim, W.G. Wamer, D. Melka, J.H. Callahan, J.J. Yin, *J. Am. Chem. Soc.* 136 (2014) 750–757.
- [29] Q.L. Chen, Y.Y. Jia, S.F. Xie, Z.X. Xie, *Chem. Soc. Rev.* 45 (2016) 3207–3220.
- [30] H.G. Yang, C.H. Sun, S.Z. Qiao, J. Zou, G. Liu, S.C. Smith, H.M. Cheng, G.Q. Lu, *Nature* 453 (2008) 638–641.
- [31] R.G. Li, F.X. Zhang, D.E. Wang, J.X. Yang, M.R. Li, J. Zhu, X. Zhou, H.X. Han, C. Li, *Nat. Commun.* 4 (2013) 1432.
- [32] R.G. Pearson, *Inorg. Chem.* 27 (1988) 734–740.
- [33] Y. Xu, M.A.A. Schoonen, *Am. Miner.* 85 (2000) 543–556.
- [34] H. Wang, H. Yao, P. Sun, D. Li, C.H. Huang, *Environ. Sci. Technol.* 50 (2016) 145–153.
- [35] J.M. Buriak, P.V. Kamat, K.S. Schanze, *ACS Appl. Mater. Interfaces* 6 (2014) 11815–11816.
- [36] A. Kudo, Y. Miseki, *Chem. Soc. Rev.* 38 (2009) 253–278.
- [37] Y. Zhang, T. Ren, *Chem. Commun.* 48 (2012) 11005–11007.
- [38] L. Davydov, S.E. Pratsinis, P.G. Smirniotis, *Environ. Sci. Technol.* 34 (2000) 3435–3442.
- [39] P. Kubelka, F. Munk, *Z. Technol. Phys.* 12 (1931) 593–601.
- [40] L. Kavan, M. Gratzel, S.E. Gilbert, C. Klemenz, H.J. Scheel, *J. Am. Chem. Soc.* 118 (1996) 6716–6723.
- [41] H.J. Zhang, G. Chen, Y.X. Li, Y. Teng, *Int. J. Hydrogen Energy* 35 (2010) 2713–2716.
- [42] P.M. Wood, *Biochem. J.* 253 (1988) 287–289.
- [43] S.N. Li, G.H. Dong, R. Hailili, L.P. Yang, Y.X. Li, F. Wang, Y.B. Zeng, C.Y. Wang, *Appl. Catal. B* 190 (2016) 26–35.
- [44] R. Hailili, Z.-Q. Wang, M.Y. Xu, Y.H. Wang, X.-Q. Gong, T. Xu, C.Y. Wang, *J. Mater. Chem. A* 5 (2017) 21275–21290.
- [45] X.J. Luo, Y.S. Liu, C.P. Yang, S.S. Chen, S.L. Tang, K. Bärner, *J. Eur. Ceram. Soc.* 35 (2015) 2073–2081.